Active learning - assisted experimental design for porous ceramic manufacturing

Jnanesh Gopale Gowda, Liam Latour, Paul Baral, Renaud Ferrier, Sébastien Saunier

Journal of the European Ceramic Society 46 (2026) 118116

Contents lists available at ScienceDirect

Journal of the European Ceramic Society

journal homepage: www.elsevier.com/locate/jeurceramsoc

Active learning-assisted experimental design for porous ceramic manufacturing

Jnanesh Gopale Gowda *, Liam Latour, Paul Baral, Renaud Ferrier, Sébastien Saunier

Mines Saint-Étienne, CNRS, UMR 5307 LGF, Centre SMS, Saint-Étienne F-42023, France

ARTICLE INFO

Keywords:
Powder metallurgy
Porous ceramics
Active learning
Classification
Permeability

ABSTRACT

Porous alumina ceramics are fabricated using the sacrificial template method to investigate the impact of two different sphere sizes, PMMA porogen (D_{50} of 80 and 163 μm) and volume fraction (up to 76 vol%) on material properties. In order to screen the viable parameter space (where samples are mechanically resistant and permeable) efficiently and to leverage the possibility to manufacture several samples in parallel, a batch active learning algorithm coupled with a data-driven model based on Gaussian process classification is developed. Complementary, a Gaussian process regression (GPR) model is developed to predict permeability trends across the viable parametric space. Both models are tested and blind-validated experimentally using unseen data. The combination of GPC and active learning offers a powerful tool for generating effective experimental plans, particularly when investigating processes with large parametric spaces.

1. Introduction

Porous technical ceramics gained significant attention and development in the 20th century, particularly from the 1970s onward, due to advancements in production techniques and their expanding range of applications [1]. Since then, they have been widely used in biomedical engineering, the automotive industries, and various industrial processes. Porous ceramics characterized by low permeability find applications in advanced engineering fields, with their performance closely tied to the features, such as porosity, pore size distribution, connectivity, and tortuosity [2,3]. By adjusting these microstructural attributes, it is possible to create ceramics that are tailored for specific functional needs. For example, applications requiring effective transport through the pore system, like bone scaffolds [4,5], microfiltration [6,7], exhaust gas filtration for capturing particulates [8], or reference standards for lab equipment calibration [9].

In addition, infiltrated ceramics created by filling a porous preform with an additional phase provide improved strength, toughness, and stability at high temperatures by minimizing open porosity, thus allowing porous ceramics to be utilized in more challenging mechanical and thermal conditions for applications like ballistics [10] and dental implants [11]. On the other hand, thermal insulation applications leverage ceramics with mainly mesoporous structures and a high degree of closed porosity, which effectively reduces heat transfer by inhibiting gas convection and radiation [12]. In summary, the pore morphology is a key factor influencing porous ceramics applications.

Several methods have been developed for creating porous ceramics, such as partial sintering [13], direct foaming [14], replica techniques [15], and the sacrificial template method [16]. Even though partial sintering provides some control over porosity, it often struggles to ensure consistent and precise pore properties. The replica technique forms thin ceramic struts along with strut pores, which results in low mechanical strength. Direct foaming methods can produce highly porous structures, but they often face challenges in achieving homogeneous pore characteristics and controlling the resulting microstructural features. On the other hand, the sacrificial template method offers a more flexible and manageable approach, allowing for precise manipulation of pore architecture.

This research investigates the application of the sacrificial template technique using PMMA spheres as a porogen for fabricating alumina-based porous ceramics. This approach provides accurate management of the pore structure, which is crucial for enhancing performance in areas such as filtration and bone scaffolding. The ratio of sacrificial material used in the process significantly affects the final density, porosity, pore size distribution, mechanical strength, and other physical properties of the final sample [17,18].

* Corresponding author.
E-mail addresses: jnanesh.gopalegowda@emse.fr (J.G. Gowda), paul.baral@emse.fr (P. Baral), renaud.ferrier@emse.fr (R. Ferrier), sebastien.saunier@emse.fr (S. Saunier).

https://doi.org/10.1016/j.jeurceramsoc.2025.118116
Received 16 October 2025; Received in revised form 12 December 2025; Accepted 24 December 2025
Available online 30 December 2025

Depending on the manufacturing parameters, particularly the quantity and nature of the porogens, the resulting sample will be fractured or remain intact, permeable or impermeable along a direction of interest. In this article, a sample whose permeability is higher than $10^{-16}m^2$ is considered permeable. The prediction of that outcome is not necessarily trivial, so it is decided to develop a data-driven classification model. More specifically, Gaussian process classification (GPC) [19] is chosen. In anticipation of the future need to explore the impact of numerous processing parameters, a batch active learning strategy is developed to guide experimental data collection. Active learning is a machine learning framework in which the algorithm selects the most informative instances from an unlabelled dataset for annotation by an oracle, typically a human expert. Active learning methods include error estimation techniques, such as Expected Error Reduction (EER), which aims to minimize the model's generalization error [20], model change methods, like Expected Model Change (EMC), which prioritize instances that would cause the most significant change to the current model if labelled [21] and uncertainty sampling, which selects instances based on label uncertainty [22]. In this article, the latter category of methods is used. Reference [23] explains the role of data and model uncertainty relating to material design in active learning. The goal is to optimize model accuracy with minimal labelled data, thereby reducing annotation costs and the number of required data points because in our case data point labelling is time-consuming and costly. More precisely it requires manufacturing the corresponding sample to observe its mechanical integrity and determining experimentally if it is permeable, independently. This process can be speed-up through batch manufacturing. This calls for a batch active learning approach, as the ones developed in [24,25].

Several Gaussian process regression (GPR) models are developed for permeability prediction in various contexts. For instance, permeability calculation from CT scan data of carbonate cores [26], heterogeneous carbonate reservoirs [27], and prediction of reservoir porosity and permeability from petrophysical well log data [28]. Additionally, GPR models have been employed in uncertainty-aware frameworks for reservoir permeability prediction using different kernels, including the Gaussian kernel [27,28]. These examples validate the suitability of GPR for permeability estimation in complex porous materials, supporting its application in the present study. A significant advantage of GPR is to estimate the prediction uncertainty in any location of the parametric domain, which has proved to be beneficial in several material science studies [29–31].

The experimental data offer valuable insights into the relationship between processing conditions and material performance and help streamline the design of porous ceramics. The research findings have the potential to enhance fabrication processes and improve the efficiency of porous ceramics in diverse industrial applications, meeting the growing demand for high-performance materials while minimizing material wastage.

In this study, we investigate the manufacturing of porous alumina ceramics utilizing the sacrificial template method, examining how the volume and size of porogen spheres influence the properties of the

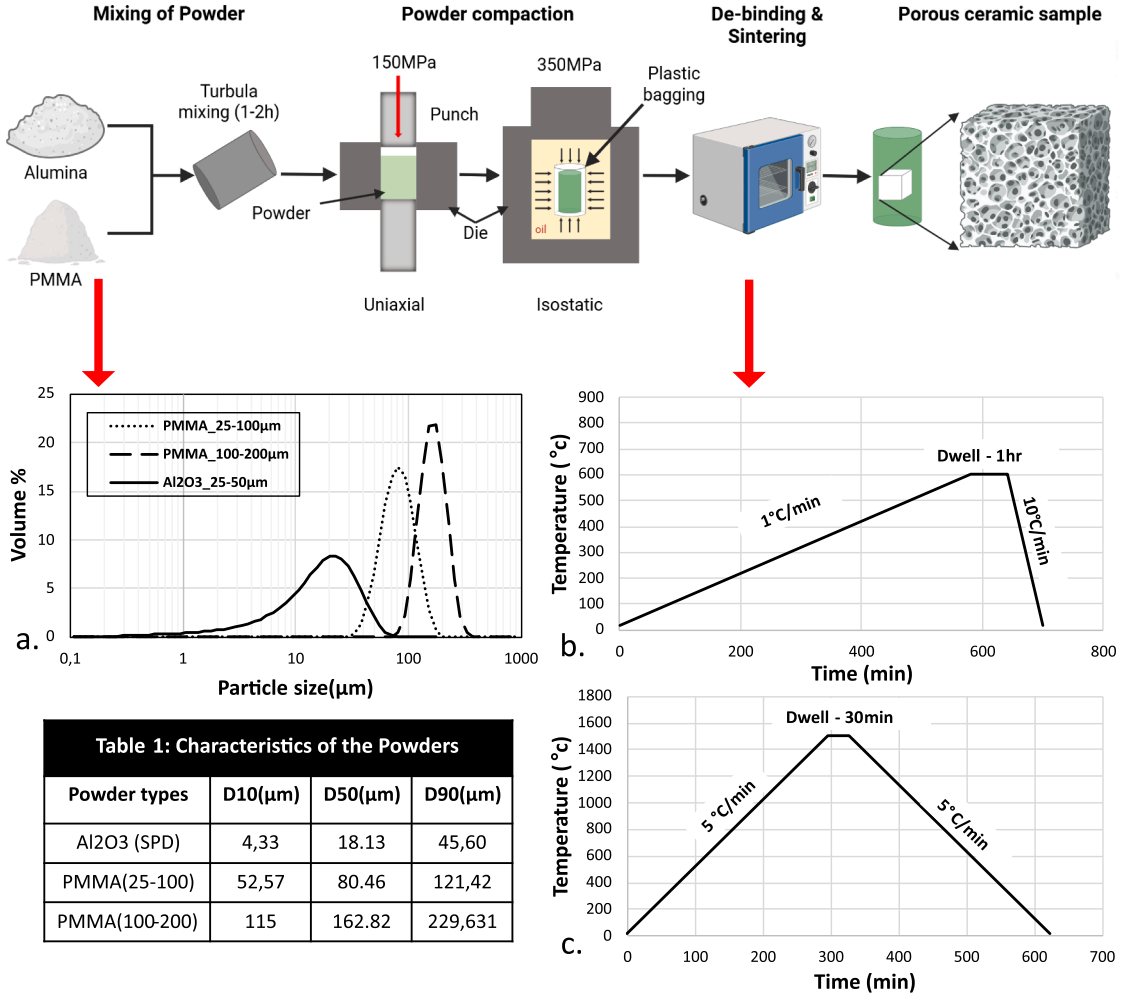

Table 1: Characteristics of the Powders			
Powder types	**D10(µm)**	**D50(µm)**	**D90(µm)**
Al2O3 (SPD)	4,33	18.13	45,60
PMMA(25-100)	52,57	80.46	121,42
PMMA(100-200)	115	162.82	229,631

Fig. 1. Sample preparation process. a) Granulometry/ Sphere atomisation diameter distribution of alumina powder and PMMA porogen used in this study, b) Debinding, and c) Sintering temperature cycles.

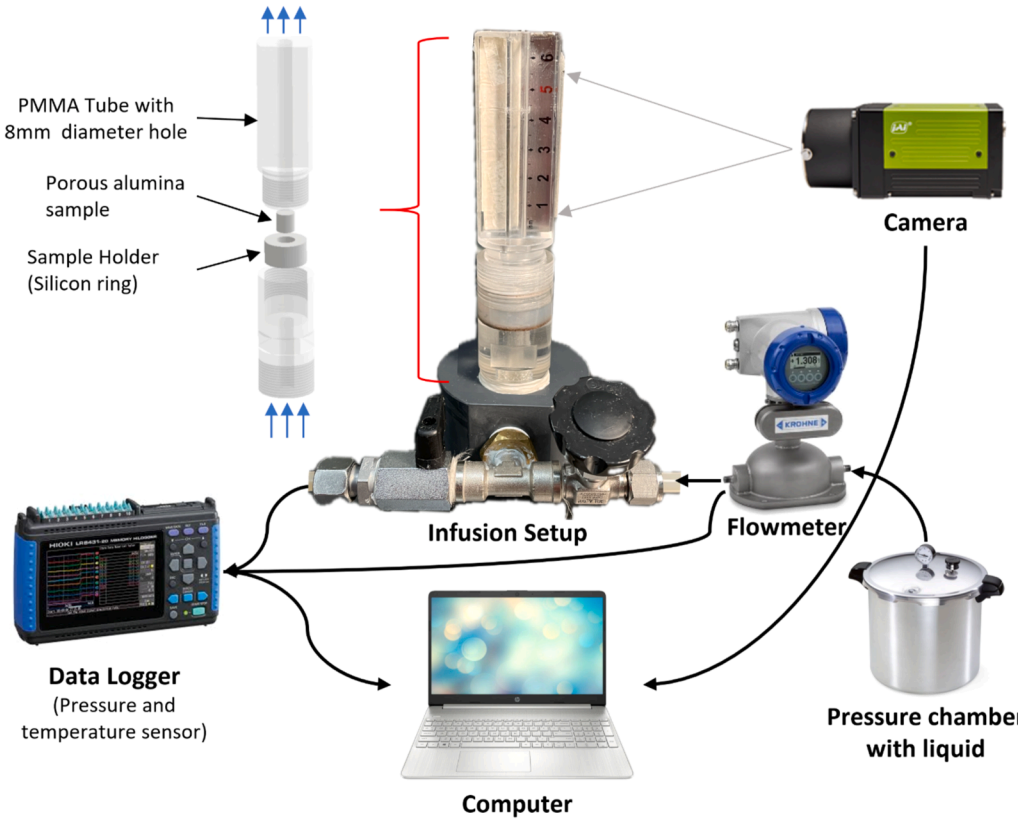

Fig. 2. Schematic of the permeability testing setup.

material. Although the sacrificial template method is mostly used for closed-pore applications. The debinding and sintering conditions were deliberately selected to preserve microcracks that contribute to pore connectivity, forming permeable structures with measurable permeability. Along with Gaussian process models to identify the process parameters and predict permeability. The final reach of this study will be to generate samples of different porosity levels to study and analysis of pore morphology and fluid dynamics within them, aiming to develop a predictive simulation model [32], but this is not addressed in this article.

2. Materials and methods

2.1. Materials & sample preparation

The two components used to produce the composite porous material are alumina and PMMA powders. Atomized alumina BA15W (Al_2O_3) from Baikowski Chimie (Poisy, France) is a high-purity α alumina spray dried powder (SPD) of BET-specific surface area of 16 m^2/g. Polymethyl methacrylate (PMMA) spheres from Diakon are provided by Lucite International (Rotterdam, Netherlands) and are used as porogen. PMMA is sieved using a Retsch digital sieve machine (AS series) equipped with 25 μm, 100 μm, and 200 μm mesh sieves to obtain two distinct particle size ranges referred to as "25–100" and "100–200" in the article, whose resulting median particle diameters (D_{50}) are approximately 80 μm and 163 μm, respectively. Particle size distribution is measured using the Mastersizer 3000, Malvern Panalytical, UK, equipped with a dry dispersion unit (Aero S). Data are processed using Mie theory with refractive indexes of 1.7659 and 1.488 for alumina powder and PMMA porogen, respectively, and their particle size distribution is illustrated in Fig. 1a. The two PMMA size ranges (25–100 and 100–200) exhibit broad and partially overlapping particle-size distributions due to the limitations of mechanical sieving. Granulometric measurements show that the overlap occurs around ~116 μm, with fewer than 20 % of the 25–100 μm fraction exceeding this value and a similar proportion of the 100–200 μm fraction falling below it.

Alumina and porogens are combined in volumetric ratios ranging up to 76 vol% of porogen and homogenized using a TURBULA mixer for approximately 2 h. The resulting composite powders are compacted under a uniaxial load of 150 MPa to form a cylindrical green compact of 12 mm diameter and 14–18 mm height using an Instron 5584 testing machine. The greens are further compressed under an isostatic pressure of 350 MPa using a Nova Swiss hydraulic machine. The green compact is then subjected to debinding using Thermolyne Furnace 6000 to remove alumina binders and porogens, creating a solid porous cylindrical sample. Debinding is performed at 600 °C for 1 h with a heating rate of 1 °C/min. Then sintered using Nabertherm lht 08/17 at 1500 °C for 30 min at a heating rate of 5 °C/min. The temperature ramp cycles are given below in Fig. 1b and c, respectively. Two samples of each mixture are generated to check the repeatability of the outcome.

2.2. Permeability testing setup

Several methods exist to measure permeability, aside from the more commonly used laboratory techniques such as the constant head and falling head permeability tests, which are typically employed to assess the permeability of soils and concrete [33,34]. One such method is the pressure drop method, where air or fluid is passed through the material to create flow. In this method, the pressure difference between the entry and exit points of the sample is measured, and the flow rate is monitored. By analysing the pressure variation at the desired flow rate, the permeability of the material can be determined [35,36].

The Darcy law describes the permeability k of a homogenized porous structure such as:

$$k = \frac{Q * \mu * L}{A * \Delta P} \quad (1)$$

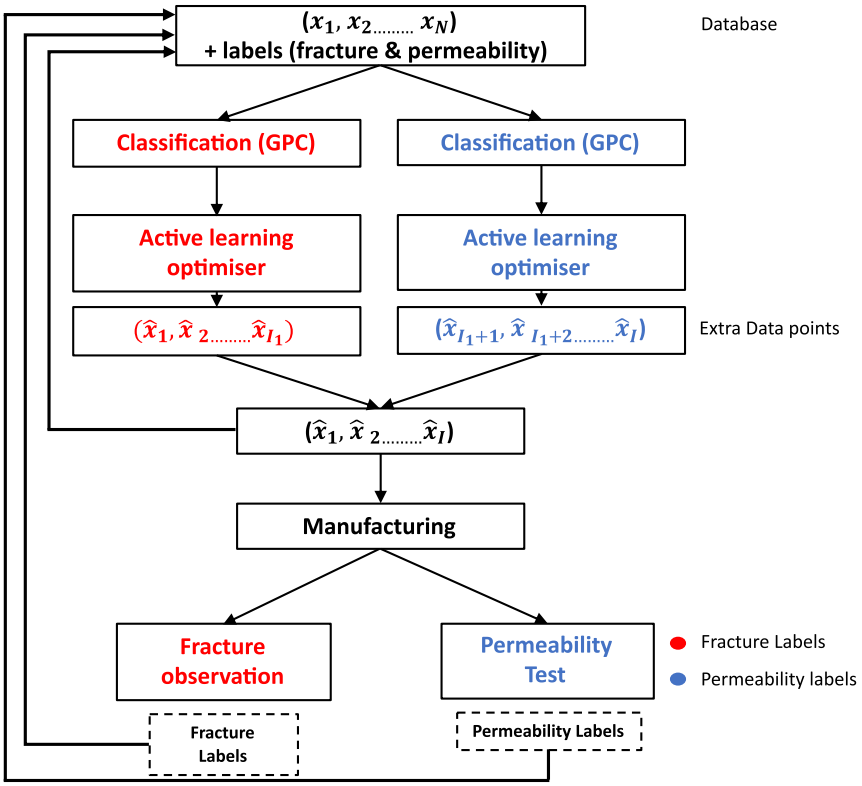

Fig. 3. Flowchart of active learning algorithm for determining the valid process region.

with k the sample permeability (m^2) and Q the volumetric flow rate (m^3/s), A the sample cross-sectional area (m^2), ΔP the pressure difference (Pa), μ the fluid dynamic viscosity (Pa. s), L the sample length (m).

Designing a permeability testing setup requires precise control over several factors, including flow rate, pressure, and fluid viscosity [37,38]. Based on these requirements, a permeability testing method has been developed. The setup schematic is illustrated in Fig. 2.

The sample is securely mounted in place using a silicon elastomer (Shore A45), which compresses the sample radially upon tightening the upper PMMA tube to the fixed lower tube and assure a perfect radial sealing of the sample. Distilled water is used as the fluid because its purity prevents pore clogging to ensure accurate and uncontaminated measurements. A 1.5 bar pressure chamber is used to pressurise the fluid, together with a valve which limits the fluid flow rate.

The pressure and temperature during the test are measured synchronously with a data logger HIOKI LR8431–20 equipped with 9 channels, each capable of handling 0–10 V inputs and 10 mA measurements. The fluid temperature is measured with a μ-thermocouple type K (whose precision is ±0.1 °C). The fluid temperature is used to adjust the fluid dynamic viscosity μ based on its actual temperature during the test. The thermocouple is placed downstream of the sample. The pressure is measured upstream of the sample with a pressure sensor Ashcroft KXF (whose precision is ±0.02 bar). The pressure difference due to the fluid flow in the sample can therefore be calculated at the end of the experiment. A camera GO-5100M-USB with a maximum definition of 2464 × 2056 pixels is used to capture the flow front position in the transparent tube at a given acquisition frequency. A calibrated scale is placed in the field of view to ensure an accurate flow measurement. A field of view of 720 × 2056 pixels and 3941 mm^2 is used, which leads to a resolution of ~30 μm/pixel.

All the non-fractured samples are tested to determine their permeability. The two ends of the tested cylindrical sample are polished using a diamond polishing disc (grits from 20 to 6 μm) for less than 2 min to enhance surface regularity and minimize the impact of the skin effect during permeability testing. In this study, we choose a permeability threshold of $10^{-16}m^2$ under which measurements are considered out of the study range (this will be abbreviated as simply "permeable" in the remaining sections). This is not due to precision error but to the long experiments' duration. Indeed, the pressure chamber used is limited to a maximum pressure of 1.5 bar, if we assume a sample with permeability of $\sim 5 * 10^{-17}m^2$ the resulting flow rate would be 0.08 mm/min and the time for the fluid flow front to reach 10 mm displacement would be approximately 2 h. By considering a permeability of $10^{-16}m^2$, the time of a test at maximum pressure is approximately 60 min, which allows several tests to be performed by day. Mass flow measurements are recorded simultaneously during the testing using a Coriolis mass flow sensor (OPTIMASS 3000 S01, KROHNE, Germany) with a precision error of less than 1 %, in order to validate the developed permeability measurement technique.

2.3. *Workflow for the active learning model construction*

The aim of the approach is to use the collected experimental data to feed a model able to predict if a given distribution of porogens will lead to a viable sample, i.e., non-fractured and sufficiently permeable for the permeability measurement. In machine learning, this task is called *classification*. Once the frontiers of the set of viable samples have been delimited, another model is built, that predicts the permeability of the sample from the porogens distribution inside this set. This second task is a regression on the permeability, and it is performed in this article as an example to show potential further analysis once the set of viable samples has been delimited.

For both classification and regression tasks, the input vector encodes the distribution of porogens used as sacrificial template. The porogens are separated into two classes (25–100 and 100–200), and the input is a 2-dimensional vector of which each component is the volumic proportion of each of these two classes. Obviously, a model could be built with more classes of porogens, and it is expected to be more accurate,

although it could be harder to train and interpret. A 2D parametric space has the advantage of making the outcome easier to display and analyse, which is beneficial for this proof of concept.

All dependencies related to the hyperparameters used for optimising the standard deviation through marginal likelihood estimation are detailed in Annex A.2. The methodology outlines the parameter selection and optimisation process applied to the predictive model. As a data-driven approach, the model's accuracy is highly dependent on both the quantity and the diversity of the input data.

2.3.1. Classification

A first classification operation is performed to determine the frontier of the set of non-fractured samples, while a second classification operation determines the frontier of the set of permeable samples. Both are done with the Gaussian process classification (GPC) algorithm described in Section 2.4, which returns as output a fuzzy indicator value (a real number in the interval [0,1]). The frontier of each set is the 0.5 isovalue of the corresponding output value.

Both classification outcomes are combined by multiplying both values (logical "and") to obtain an indicator value that represents the viability of the sample. The 0.5 isovalue of that last indicator is the frontier of the set of viable samples.

Note that it is possible to achieve the classification directly with the "viable" and "non-viable" classes. However, our practical tests suggest that this direct approach is less effective (in the sense of accuracy and required data quantity) than the above-described one. This is probably linked to the fact that each classification model optimizes its hyperparameters through the maximal marginal likelihood method. Having one model dedicated to fracture and the other to permeability makes them able to optimize their hyperparameters independently and thus to have a higher overall likelihood.

GPC is not a classical approach, and the one used in this study is a simplified version usually found in the literature, which is why it is described in Section 2.4.

2.3.2. Multipoint active learning

The input data x is a vector of $\mathbb{R}^2$ that contains the volume fraction of each of the two classes of porogen used (25–100 and 100–200). However, the classification approach is expected to be more useful in cases where the number of parameters of the process is higher, which makes the choice of the dataset not trivial by hand.

This is the reason why the development of an active learning algorithm is deemed useful. This algorithm, mathematically described in Section 2.4.2, analyses the outcome of the classification model to determine the best positions, in the parametric space, where new data points would improve the model at best. For practical reasons, it is more convenient to manufacture samples by batches rather than one-by-one, motivating the need for a multipoint (or batch) active learning method.

The full active learning workflow consists in adding iteratively batches of points to enrich the model. These points are labelled through the manufacturing of corresponding samples and the evaluation of permeability and fracture, then incorporated into the database. This addition and labelling of a batch will be referred to as an iteration of the active learning algorithm. There are two classification tasks (fracture and permeability) done on the same database. At each iteration, the active learning optimiser computes data points dedicated to each of the classification tasks. Once labelled, those points are added together to the database, Fig. 3 shows the Flowchart of the active learning algorithm for fracture and permeability.

2.3.3. Permeability regression

The data-driven prevision of permeability inside the viable region of parametric space is done through Gaussian process regression, which is a very classical method of which main aspects are given in Annex A. The only subtility in this part is that, as the experimental uncertainty on the measurement seems to be relative, the permeability can be assumed to follow a log-normal probability distribution law. Hence, its logarithm is assumed to obey a Gaussian distribution law, and the regression is actually done on this logarithm rather than the permeability itself.

2.4. Gaussian process classification

Gaussian process classification (GPC) [19] extends Gaussian process regression (GPR) to binary classification by modelling class probabilities through a non-parametric, probabilistic approach. It maps input features to a latent space and applies a sigmoid function to predict class probabilities while quantifying uncertainty. This makes GPC particularly useful for small or sparse datasets, as it provides both predictions and uncertainty estimates.

Additionally, GPC captures complex patterns that methods like Random Forest [39] and Support Vector Networks [40] might overlook. This enhances the predictive potential of GPC. Scikit-learn [41], is an open-source machine learning library for Python, widely used for data analysis, modelling, and machine learning tasks. It is utilized in this work to pre-prototype the code and compare the GPC method with other classification approaches. However, the end results displayed in this article are obtained with a direct re-implementation of the GPC method [42], which is required for developing the active learning algorithm [43].

2.4.1. Classification through Gaussian process regression

Following the idea of [19], the classification is performed by applying a sigmoid function to a latent variable, which is subject to GPR.

$$c = f(x) = g(\mathrm{y}) with y = \mathrm{h}(\mathrm{x}) \tag{2}$$

where $c \in [0,1]$ represents the membership to the default class. In this study, for the presence of cracks, 0 represents fractured samples, and for the permeability, 0 represents impermeable samples. $\mathrm{y} \in \mathbb{R}$ is the latent variable. The function g is the sigmoid, and the function h is the latent function, obtained by GPR.

$$g(y) = \frac{1}{1+e^{-y}} \tag{3}$$

If the amplitude of the latent variable y is sufficiently big, c tends towards a Boolean variable.

In [19], the authors establish the formula for the Bayesian inference through the sigmoid function and derive the algorithm for GPC which is implemented in Scikit-learn. This algorithm is non-explicit in the sense that it requires the resolution of a nonlinear problem through Newton's method. The multipoint active learning strategy detailed in Section 2.4.2 does not seem to be directly applicable to this GPC method. This is why, in the present study, a more sequential and naiver version of GPC is used. This approach consists of writing explicitly the latent variable y by attributing pre-determined and "sufficiently high" values $\pm\ \xi$ to the points of the dataset and performing Gaussian process regression on this variable. The sigmoid function is then applied to the output to obtain c. In our implementation, $\xi = 10$ (see Annex B.1 for details on this choice).

The class variable c can be interpreted in the framework of fuzzy logic as the probability of the point belonging to the 1 class. This is how a margin where the confidence is lower than 90 % can be defined as the set of points for which $\mathrm{c} \in [0.05,0.95]$. This margin will be referred to as the uncertainty margin in the remainder of this article.

A comparison between our approach and the reference method of [19] is expected to turn in favour of the latter because of its sound mathematical foundations. This is why a perspective of our work is to adapt the batch active learning strategy to it. Nevertheless, a comparison between our simplified GPC formulation and a scikit-learn implementation based on [19] is provided in Annex F, confirming that both approaches yield nearly identical decision frontiers while exhibiting minor differences in stability at the two frontiers.

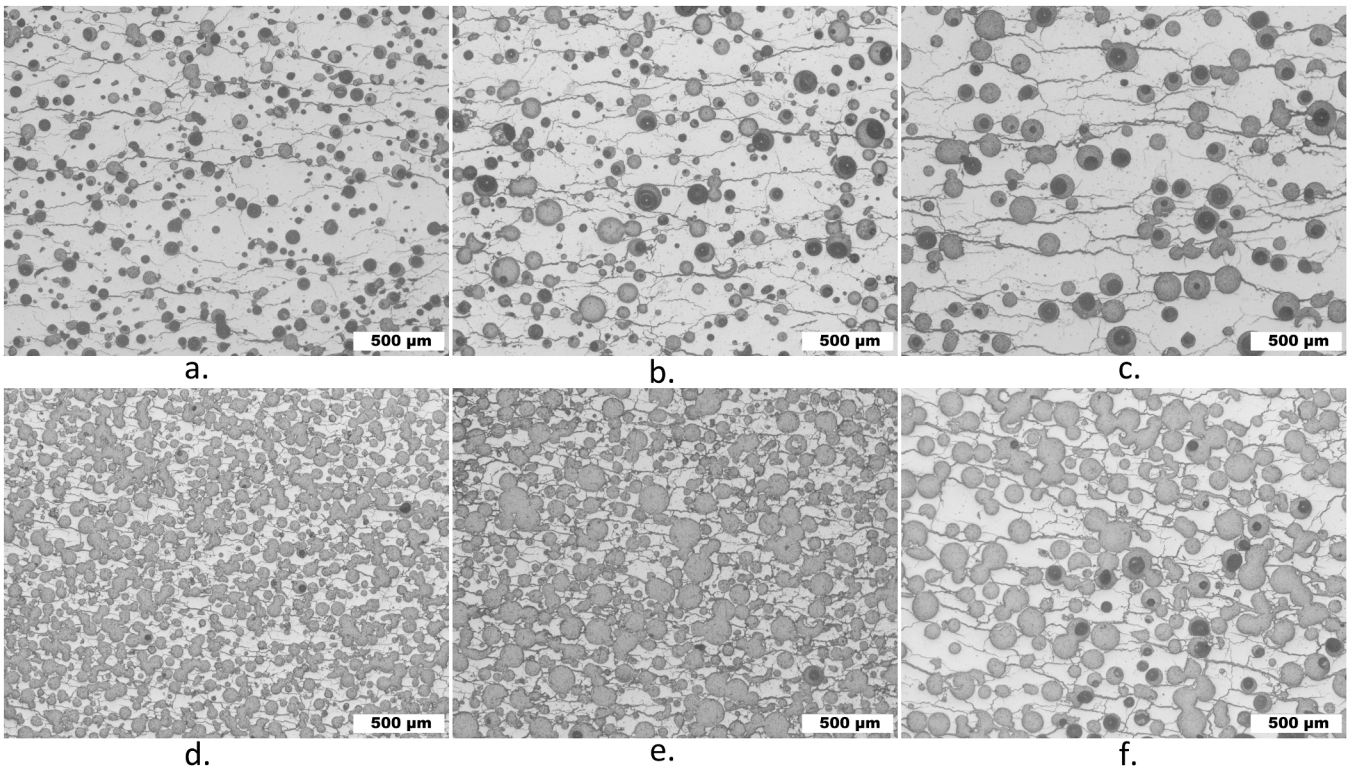

Fig. 4. Optical images of cross sections aligned to the sample axis: sample elaborated a) with 30 vol% of 25–100 PMMA porogen, b) with 30 vol% of 25–200, c) with 30 vol% of 100–200, d) with 60 vol% of 25–100, e) with 60 vol% of 25–200, and f) with 60 vol% of 100–200. Alumina appears as light grey, resin as dark, and unfilled pores as black. (25–200 is an equal volume mix of 25–100 and 100–200 porogen).

2.4.2. *Multipoint active learning strategy*

Given an initial and very sparse set of labelled data points $\{x_n\}_{n=1..N}$ the task of the Active Learning algorithm is to find the set of points $\{\hat{x}_i\}_{i=1..I}$ to add to the database in order to enrich the model at best. The term "best" has to be defined in sense of a certain cost-function. The chosen approach optimizes a cost function balancing uncertainty reduction and sample diversity. This combination aims at improving model accuracy with fewer labelled samples, reducing experimental

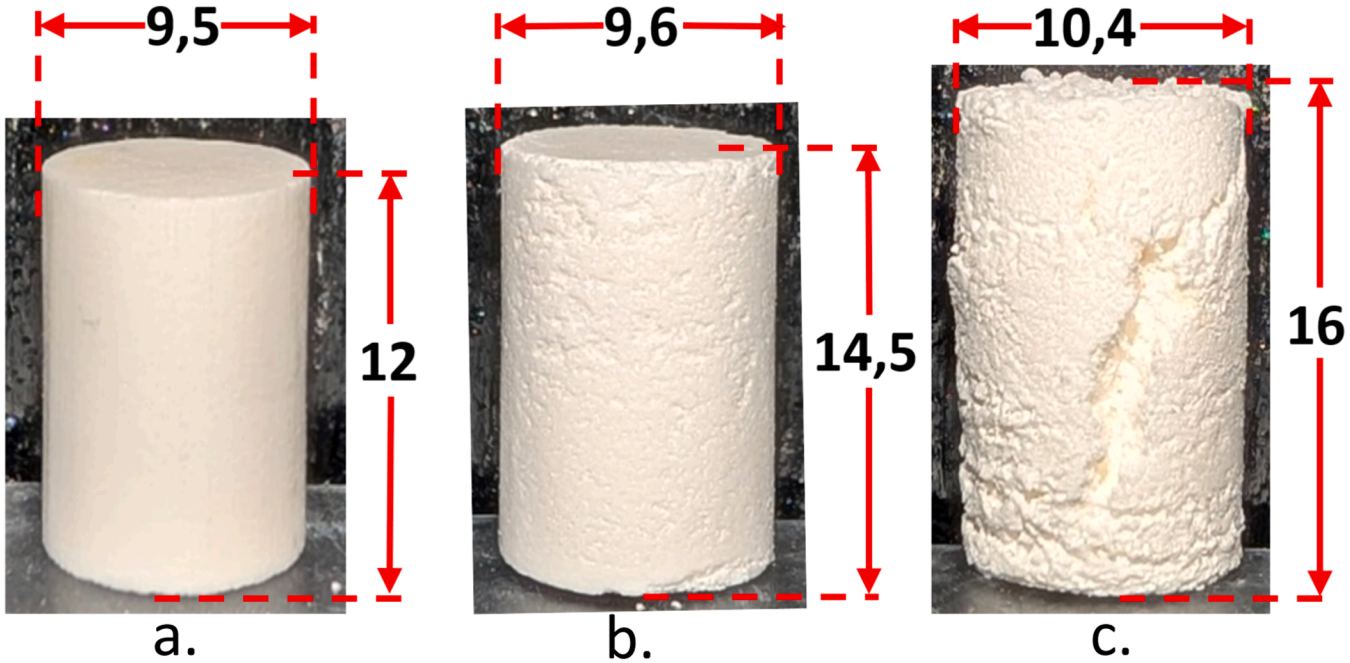

Fig. 5. Sintered porous ceramic samples elaborated with PMMA porogen volume of a) 30 vol% of 25–100, b) 20.70 vol% of 25–100 and 41.53 vol% of 100–200 and c) 76 vol% of 25–100. (*Measurements are in mm scale).

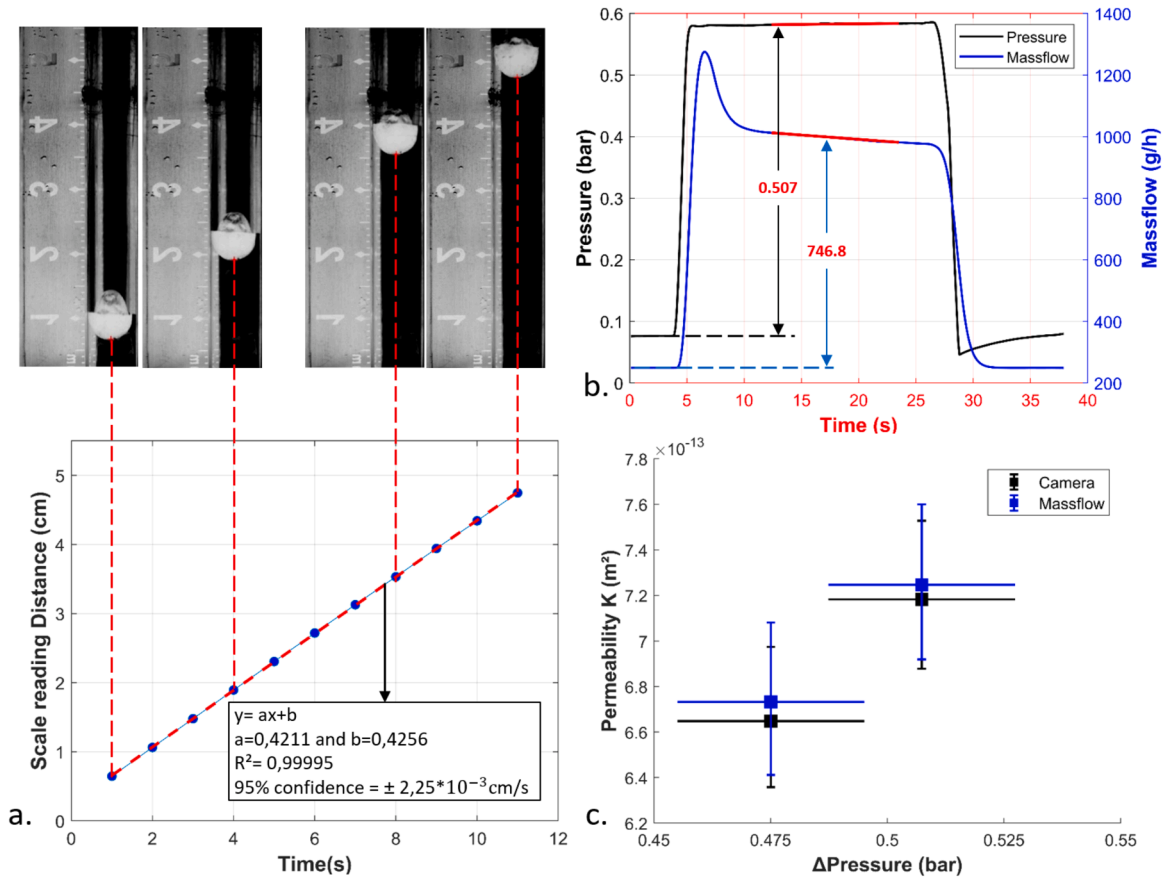

Fig. 6. a) Image processing of the permeability test in MATLAB to calculate the flow velocity for the 60 vol% PMMA porogen sample. b) Variation of flow pressure and mass w.r.t. time during one of the permeability tests. c) Permeability K of the sample for two tests. The horizontal error bar represents the uncertainty from the pressure gauge, while the vertical error bar corresponds to uncertainties in velocity and fluid viscosity for the developed image-based method, and to mass flow meter and fluid viscosity errors for the mass flow method.

costs.

The set of points $\{\hat{x}_i\}_{i=1..I}$ minimizes the following cost function φ:

$$\varphi(\{\hat{x}_i\}_{i=1..I}) = \underbrace{\frac{1}{2\xi}\sum_{i=1}^{I}\left(h(\hat{x}_i)\right)^2}_{\varphi_\xi} + \underbrace{\frac{\kappa}{2}\sum_{i=1}^{I}\sum_{n=1}^{N} exp\left(-\frac{\|\hat{x}_i - x_n\|}{\lambda}\right) + \frac{\kappa}{2}\sum_{i=1}^{I}\sum_{j=1}^{I} exp\left(-\frac{\|\hat{x}_i - \hat{x}_j\|}{\lambda}\right)}_{\varphi_\kappa} \tag{4}$$

φ_ξ is a fitness cost: low if the point is close to the zero iso-value of the latent function h, which is the frontier between the two classes.

φ_k is an exploration cost: high if the points resemble points already in the database. It is the Frobenius norm of the intercorrelation matrix between the new samples and the already existing samples.

φ is optimised through a gradient algorithm with multiple initial guesses to overcome local minima. Note that this approach is not optimal and might benefit from a dedicated non-convex optimization method.

Hyperparametersofthemethod| *λ is the correlation length*
K is the weighting term for exploration
ξ is the value ± 10

2.4.3. Comparison with existing frameworks

The proposed approach shares technical similarities with Bayesian Optimization (BO) [44–46] and Reinforcement Learning (RL) [47,48], as all three methods focus on the selection of new data points to best match a target. BO, in particular, is closely aligned with our method through its use of surrogate models like Gaussian Process Regression (GPR) and Gaussian Process Classification (GPC). The developed batch active learning framework, however, distinguishes itself from it in several ways:

First, concerning the purpose of the approach, BO and RL focus on maximizing an objective function to determine the material composition that maximizes the desired property. In contrast, our batch active learning strategy aims to enhance the predictive model itself by selecting the most informative points to label. The objective of our model is to identify the range of samples that are mechanically resistant and permeable, rather than only placing the extremes (minimum or maximum) of permeability for mechanically resistant samples.

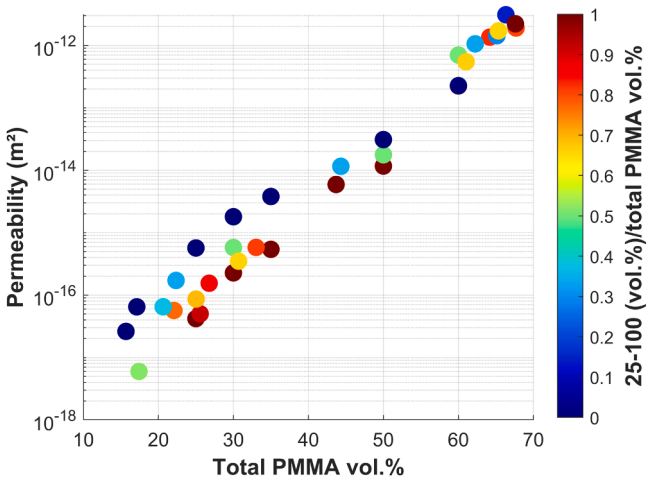

Fig. 7. PMMA vol% vs permeability.

Second, BO and RL frameworks are mostly sequential or one-by-one prediction. Although batch extensions seem to be possible in the two frameworks, our method is explicitly designed for batch querying because we apply it to experimental data, contrary to BO, which is usually applied to data obtained through computations.

To conclude, the approach proposed is very close technically to BO, with the algorithmic differences between them being nearly anecdotal. It would probably not be very hard to transform our code into a BO code, and vice versa. Both methods, however, have quite different objectives that drive those technical differences.

3. Results

3.1. Sample microstructure

The effect of porogen vol% and sphere size on the microstructure is examined using an inverted optical microscope X51. The micrographs in Fig. 4 reveal distinct differences in pore characteristics between samples elaborated with 30 and 60 vol% of porogen, using 25–100, 25–200 (equal mixture of 25–100 and 100–200) and 100–200. During debinding, PMMA burnout generated microcracks, the morphology of which depends on the heating rate [49]. These microcracks subsequently formed a connecting network between the pores. Prior to imaging, the samples are vacuum-infused with Epothin 2 resin to prefill the pores and ensure high-quality polishing. In the micrographs, alumina appears as light grey, resin as dark grey, and unfilled pores as black. After debinding and sintering, the 30 vol% porogen samples (Fig. 4a, b & c) exhibited low porosity and limited connectivity, whereas the 60 vol% porogen samples (Fig. 4d, e & f) showed higher porosity with improved interconnectivity. This trend is also visible through the grayscale of pores, as there are many unfilled pores in the 30 vol% 25–100 (Fig. 4a) than on the 60 vol% 25–100 (Fig. 4d).

Table 2
Initial arbitrary mixture samples manufactured for data collection for the model.

Sample no.	25–100 vol%	100–200 vol%	Fractured	Permeable
1	0	0	No	No
2	25	0	No	No
3	0	25	No	Yes
4	30	0	No	Yes
5	15	15	No	Yes
6	0	30	No	Yes
7	35	0	No	Yes
8	0	35	No	Yes
9	50	0	No	Yes
10	25	25	No	Yes
11	0	50	No	Yes
12	60	0	No	Yes
13	30	30	No	Yes
14	0	60	No	Yes
15	32,5	32,5	Yes	Yes
16	0	70	Yes	Yes

3.2. Fracture results

The size of porogen spheres used in the fabrication of porous ceramics has a high impact on the mechanical integrity, which tends to decrease with increasing porogen size [50] and directly contributes to the fracture of the sample. The mechanical integrity (fracture) of alumina ceramics fabricated using the sacrificial template method is significantly influenced by the ratio of porogen. An increase in the porogen volume leads to elevated porosity in the ceramic [51]. These voids formed during porogen removal act as stress concentrators, thereby decreasing the mechanical integrity and increasing susceptibility to crack initiation and propagation. In this study, fractured samples are defined as those exhibiting large external cracks, as in Fig. 5c. Internal cracks are excluded from analysis due to challenges in characterization and accessibility. As observed in Fig. 5, an increase in the volume of porogen leads to a deterioration in the surface quality of the ceramic cylinder, ultimately resulting in fracture at a certain volume percentage.

3.3. Permeability test data analysis

During the test, the flow velocity, pressure, temperature, and mass flow are recorded utilizing a mix of image analysis, flow pressure, temperature, and mass flow data acquisition. A suitable MATLAB code is developed in-lab to analyze the recorded data. Fig. 6 shows an example of permeability measurements made on 60 vol% porogen, consisting of equal percentages of 25–100 and 100–200.

Flow velocity is estimated by placing a floating sphere in the tube above the sample. A manual point is selected on the first image of the video to identify the center of the sphere. The vertical line passing through this point is used to compute the position of the bottom of the sphere at each frame. When the grayscale values along this line exceed 40 % of the maximum intensity, their positions are detected, and the first occurrence corresponds to the bottom of the sphere. The detected points are expressed against time, and a linear regression is fitted to calculate the flow rate during the test. The R^2 obtained for all measurements is always higher than 0.99, which confirms the hypothesis of constant flow rate (see Fig. 6a).

Pressure and mass flow variation are recorded using a Hioki multimeter. Fig. 6b shows the evolution of mass flow rate and pressure as a function of time. The red parts on the curves highlight the steady state zone during the test, which is where ΔP and mass flow are considered for calculation. The thermocouple measurement is also recorded during the test to adjust the fluid viscosity. Finally, Fig. 6c shows the permeability measurement of the sample from the image-based method and from the mass flow meter. The average values are $6.97 * 10^{-13} m^2$ and $6.99 * 10^{-13} m^2$, respectively corresponding to a relative difference of less than 1 %. This close agreement helps to validate the developed testing and processing method. The horizontal error bar represents the uncertainty from the pressure gauge, while the vertical error bar corresponds to uncertainties in velocity and fluid viscosity for the developed image-based method, and to mass flowmeter and fluid viscosity errors for the mass flow method. The permeability trends presented in Fig. 7 illustrate the influence of using the two porogen-size ranges and vol% on the resulting permeability values. The colorscale represents the relative proportion of 25–100 porogen type over the total porogen volume. It is interesting to see that the data are not superimposed into a single master-curve, which means that total porogen volume does not pilot the permeability alone. Particularly in the left part of the curve,

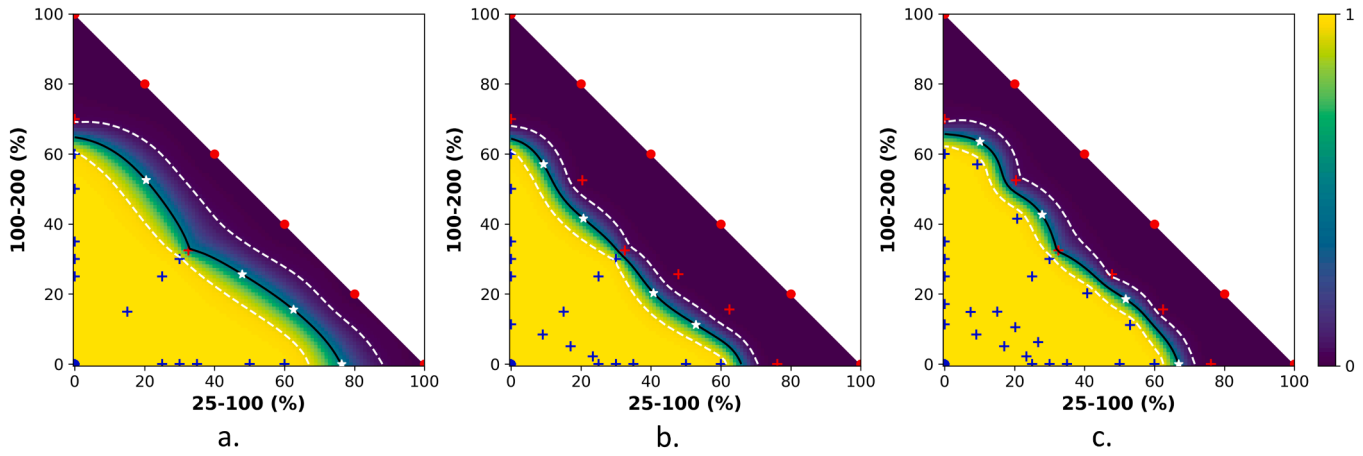

Fig. 8. Fracture determination points of the model's interest, a) Iteration 0, b) Iteration 1, and c) Iteration 2, along with uncertainty margin. (In the plots, points in red = fractured, blue = non-fractured, white = model proposed samples, and plot bar 1 = sample is not fractured & 0 = sample is fractured).

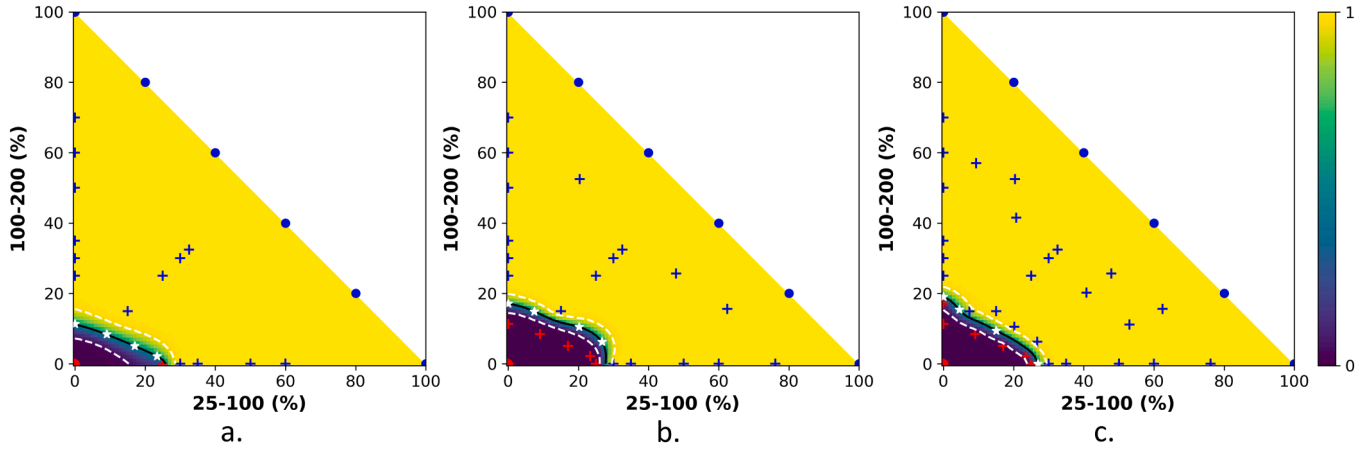

Fig. 9. Permeability determination points of the model's interest a) Iteration 0, b) Iteration 1, and c) Iteration 2, along with uncertainty margin. (In the plots, points in red = non-permeable, blue = permeable, white = model proposed samples, and plot bar 1 = sample is permeable & 0 = sample is not permeable).

where the higher the percentage of small porogen, the lower the permeability. This relation does not seem to hold for the entire porogen volume range. The role of the developed regression model is to quantify the complex interplay between porogen volume and sizes.

3.4. Model construction and predictions

To develop a data-driven fracture prediction model, it is crucial to provide a sufficient range of experimental data to allow the model to learn and predict fracture behavior at various alumina and porogen vol %. Arbitrary mixture samples as shown in Table 2, are produced with porogen content ranging from 0 to 70 vol%. Experimental results indicated that the samples produced with the two different porogen sphere size mixtures remained intact at 60 vol%. However, fractures are observed with samples of 70 vol% of 100–200 and at 65 vol% of an equal mix of 25–100 & 100–200 porogens.

GPR is sensitive to the mean of data values. At the initialization of the active learning process, to deal with unbalanced data sets (with way more points of one class than the other), it is thus necessary to introduce fictive data points at the physically defined extremes (e.g., 100 % of alumina or PMMA). The number itself (six points on each side) is chosen as sufficient for the frontier not to meet the 100 % PMMA nor the 100 % alumina extremes. That being stated, it is possible to run the process without those fictive points. The results are detailed in Annex C of the supplementary material.

Fictive data points can be identified as red disks at a 100 % range and blue disks at 0 % in Figs. 8 and 9, while the samples that are fabricated are represented by crosses " + ". The uncertainty margin (zone where

Table 3
Iteration 0 determination points.

Sample no.	25–100 vol%	100–200 vol%	Fractured	Permeable
17	20.36	52.52	Yes	Yes
18	62.44	15.61	Yes	Yes
19	47.82	25.68	Yes	Yes
20	76.14	0	Yes	Yes
21	23.4	2.15	No	No
22	0	11.32	No	No
23	16.99	5.08	No	No
24	9.01	8.39	No	No

Table 4
Iteration 1 determination points.

Sample no.	25–100 vol%	100–200 vol%	Fractured	Permeable
25	52.99	11.19	No	Yes
26	9.33	56.99	No	Yes
27	20.70	41.53	No	Yes
28	40.77	20.24	No	Yes
29	0	17.11	No	No
30	26.75	6.28	No	Yes
31	7.43	14.91	No	Yes
32	20.20	10.48	No	Yes

Table 5
Permeability test results.

Sample no.	25–100 vol%	100–200 vol%	Experimental Permeability (m^2)	Sample No.	25–100 vol%	100–200 vol%	Experimental Permeability (m^2)
2	25	0	4,20E-17	15–20 are fractured			
3	0	25	5,60E-16	21	23,41	2,15	5,01E-17
4	30	0	2,25E-16	22	0	11,33	-
5	15	15	5,75E-16	23	16,99	5,08	5,67E-17
6	0	30	1,78E-15	24	9,02	8,4	5,98E-18
7	35	0	5,31E-16	25	52,99	11,19	1,36E-12
8	0	35	3,67E-15	26	9,33	57	3,09E-12
9	50	0	1,13E-14	27	20,7	41,53	1,06E-12
10	25	25	1,74E-14	28	40,77	20,25	5,46E-13
11	0	50	3,02E-14	29	0	17,12	6,48E-17
12	60	0	2,20E-13	30	26,75	6,28	5,81E-16
13	30	30	6,97E-13	31	7,44	14,91	1,72E-16
14	0	60	2,17E-13	32	20,21	10,49	3,49E-16

the latent variable is in the interval $[0.05, 0.95]$ and the confidence in classification is lower than 90 %) is depicted by the white dashed line in the active learning plots.

3.4.1. *Fracture prediction iteration*

The model is initially trained using data from *Table 2*. Based on the initial database, the GPC is run, and the batch active learning algorithm proposes four additional points to be tested. These points are listed in *Table 3* from sample nos 17–20, and are represented as white stars in *Fig. 8* a. They are identified by the model as the most beneficial for reducing its uncertainty, i.e., enhancing its prediction ability of the fracture limit as described in Section 2.3.2. Ceramic samples are manufactured with the mixture of porogen vol% listed in *Table 3*. Fracture is observed in all 4 samples. The results are then added to the database to refine the classification model.

After updating the database, a second iteration of the algorithm is performed to give four new mixtures, to give four new mixtures of porogen vol% as shown in *Table 4* from 25 to 28 and white stars in *Fig. 8* b. Interestingly, the four different mixture ratios remained non-fractured. *Fig. 8* c shows the classification model at the end of the process, the new proposed points are not fabricated. In the last iteration, fracture boundary shifts toward higher vol%. Also, we can see that samples manufactured with the 25–100 breaks at slightly higher vol% compared to 100–200, highlighting the effect of porogen size on material fracture resistance. As shown in *Fig. 8* a – c, the margin width decreases when additional data points are introduced within it.

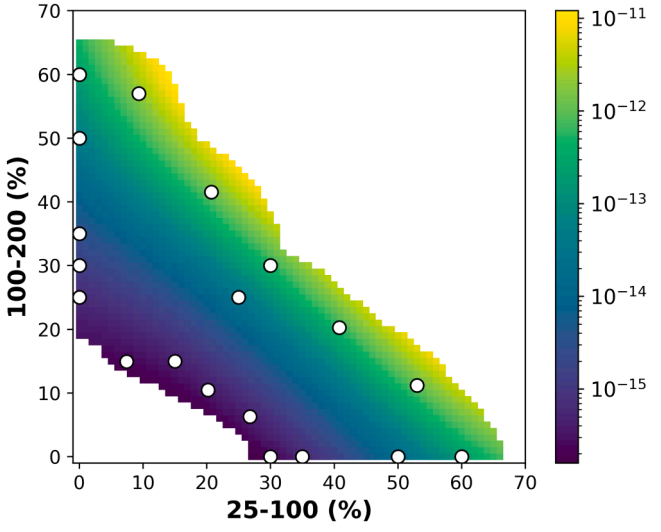

Fig. 10. Permeability map obtained from the GPR model trained with the samples illustrated as blue crosses (plot bar represents the permeability range). Only the valid process region is shown here.

3.4.2. *Permeability prediction iteration*

From the initial testing data, the impact of porogen size can be clearly identified on the sample's permeability, i.e., the 25 vol% porogen sample of 100–200 porogen has a permeability higher than the set limit while the 25–100 is comparatively 40 % lower. As there is no sample between 0 and 25 vol% porogen, the model proposes a batch of points in this range. Those points are 21–24 in Table 3 and are also shown as the white stars on Fig. 9a. Similar to fracture prediction, the iteration 0 results update is used to generate one more (or two more) iteration. Upon implementing these results in the model, a new set of points is proposed as 29–32 in Table 4 and are shown in Fig. 9b. Out of the 4 mixtures, only sample 14 is not permeable. After updating these results, in the GPC model optimisation, the influence of porogen size on permeability can be clearly identified in Fig. 9c, which also contains new iteration points in white stars that are not fabricated. In Fig. 9, we can clearly see the decrease in the uncertainty margin as the model gets more data inputs.

3.5. *Permeability regression model*

Following the classification step, the non-fractured samples from the initial dataset and the 2 iterations are subjected to permeability measurements. Among these, the samples that are permeable are selected as the training dataset for the regression model, as summarized in Table 5. Each data point in this dataset represents a distinct combination of porogen size and vol%, together with the corresponding permeability value. The GPR framework is employed to model the complex, non-linear relationships between the processing parameters and the resulting permeability. In addition to mean predictions, the advantage of the model is to get an estimation of the associated uncertainty. Fig. 10 shows the regression model result as a permeability map in the valid process region.

4. Discussion

A novel methodology to help construct a frugal experimental plan for multi-parameter processes is developed. Experimental findings reveal a distinct pattern showing a clear and anticipated trend that increasing porogen volume typically improves the permeability of the material while decreasing the mechanical integrity. Also, increasing porogen size decreases the mechanical integrity [50,52] and increases the permeability property of the porous material [53,54]. The fact that our results match this well-known trend tends to validate the proposed methodology.

The parametric influence can be observed through the asymmetry in the models' results. Fig. 11a shows that the combination of the upper boundary for fracture (Fig. 8c) and the lower boundary for permeability (Fig. 9c) results in the valid process region.

Before the active learning algorithm is run, model uncertainty is mostly epistemic, indicating a deficiency in knowledge or understanding

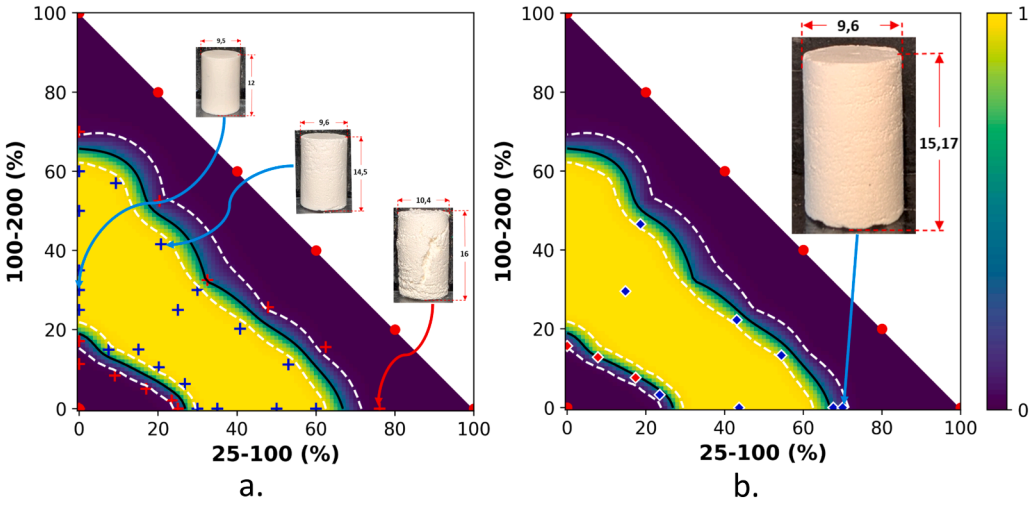

Fig. 11. Plot showing the range where the samples are a) not fractured and are permeable, and b) additional points in diamond shape that are fabricated during the model development, that fall within the uncertainty margin. (In the plots, points in red = non-permeable or fractured, blue = non-fractured or permeable, and plot bar 1 = sample is not fractured and permeable, 0 = sample is fractured or not permeable; sample measurements are in mm scale).

Table 6
Validation point.

Sample no.	25–100 vol%	100–200 vol%	Fractured	Permeable	Experimental Permeability (m^2)
33	54.41	13.27	No	Yes	1,90E-12
34	18.61	46.52	No	Yes	1,38E-12
35	67.60	0.00	No	Yes	2,21E-12
36	43.07	22.26	No	Yes	1,69E-12
37	0	15.673	No	No	2,62E-17
38	23.50	3.26	No	Yes	1,54E-16
39	7.79	12.84	No	No	6,49E-17
40	17.36	7.67	No	No	8,63E-17
41	43,69	0	No	Yes	5,91E-15
42	14,78	29,54	No	Yes	1,14E-14

that can be diminished through better information. As additional data is collected, this uncertainty transitions to aleatoric, arising from the randomness or variability present in the process [55]. The uncertainty margin is particularly meaningful in the characterization of porous ceramics, where stochastic factors such as the agglomeration or distribution of porogen can influence fracture and permeability behavior of the material, making uncertainty thresholds vital for successful model training.

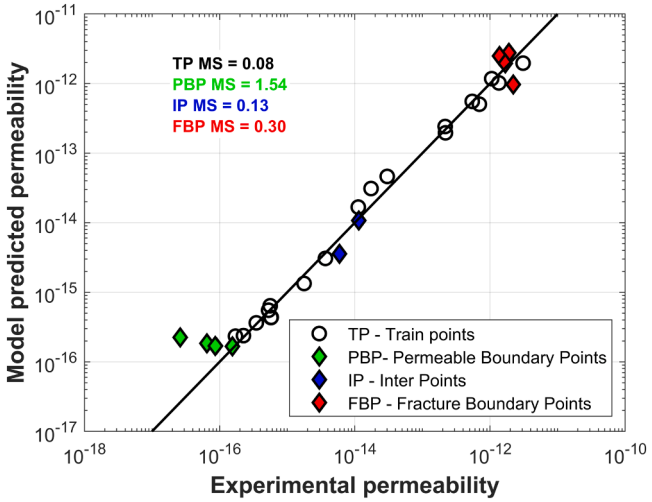

Fig. 12. Comparison plot of the experimental and GPR predicted permeability, where MS is the mean squared value.

The data density at the boundary is too limited to reliably define irregularities of characteristic length smaller than ~10 % on the curve. In particular, the small irregularities seen in Fig. 8c are clearly artificial features created by the data points themselves. But the classification model comes with its uncertainty zone, whose purpose is to inform the user of this limited reliability at small scales. The goal of our development is to provide a tool to create a model with controlled reliability, which can be high or low depending on the user's willingness to provide more or less data points.

However, a very important point is that it is not possible to get the width of this uncertainty zone to shrink towards zero. As uncertainty transitions from epistemic to aleatoric when the number of data points increases, it will ultimately tend towards an asymptotic value linked to intrinsic material variability, particularly the porogen content and its distribution. Further details are in Annex D of the supplementary material.

To evaluate the model in the uncertainty margin, a set of validation points is proposed manually as given in Table 6. Fig. 11b shows them as diamond-shaped arbitrary mixture points. These points are not included in the model's database. A 70 vol% of 25–100 sample confirms the effect of porogen size on the mechanical integrity of the porous ceramic. Even though the sample seemed to be non-fractured, the surface shows uneven surface quality as shown in Fig. 11b. Also, the diamond points in the lower mixture ratio fall close to the contour, and their permeability values are approximately ±20 % of our set limit. The above observations might indicate that in the uncertainty margin, the results are aleatoric, and thus not reproducible from a process point of view. This is the reason why both types of points still lie within the uncertainty margin. The width of the uncertainty margin is approximately 4.5 and 3.5 vol% at the fracture and permeability end of the domain,

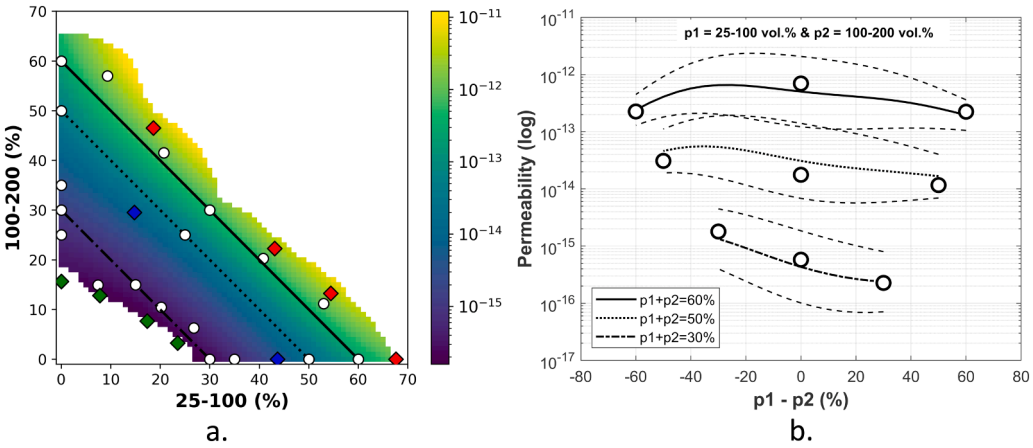

Fig. 13. a) Distribution of the database (as '+' in black and 'o' for 30,50, & 60 vol% points) and validation points (as diamond shapes) on the valid process region, with diagonal lines indicating 30, 50, and 60 vol% porogen (plot bar represents the permeability range). b) Experimental (dark dots) and predicted (solid lines) permeability values of the 30, 50, and 60 vol% porogen samples shown in green, blue, and red, respectively. The experimental standard deviation is smaller than the dot size and thus not visible, while the dashed lines ('– –') represent the standard deviation of the predicted permeability.

respectively. This corresponds to a valid process region (yellow region) in Fig. 11, where the samples are non-fractured and permeable. These low margin levels demonstrate good control over the manufacturing process.

Additional leave-one-out tests, presented in Annex E, further demonstrate how the decision boundary responds to the presence or absence of individual data points and confirm the stabilizing effect upon adding new data points at the process boundaries.

It must be noted that the present study focuses on determining the bounds of the experimental domain, which leads to a high density of data at the edges of this domain. In that sense, the resulting database presents a study that is less suited for regression of permeability inside the domain since less data are available.

Following the GPC results, the predictions obtained by the developed GPR model are illustrated in Fig. 12, where a direct comparison between model prediction and experimental permeability is proposed. The mean squared error (MS) for the training dataset points (TP – permeable samples from 1 to 32) is relatively low at 0.08, indicating an excellent fit within the trained domain. However, the model exhibits higher prediction errors at the extreme regions of the valid process domain, particularly for the Fracture boundary points (FBP – samples from 33 to 36) and Permeable boundary points (PBP- samples from 39 to 40). For PBP, the model tends to overestimate permeability, yielding a high MS value of 1.54. This poor prediction arises because these points lie outside the valid process region where the GPR model was not trained. The MS for the fracture boundary points is 0.30. When test points lie far from the training domain, the model tends to revert toward the global mean of the training data, producing predictions closer to the average value rather than capturing extreme experimental variations. In contrast, Interpolated points (IP – samples 41 & 42) located near the central region of the permeability classification range are well-covered by the training data, yielding a much lower MS of 0.13. This highlights the importance of ensuring that test points lie within or close to the trained region to maintain accurate predictions and avoid bias toward the dataset mean.

From both experimental permeability measurements and predictive modelling, a clear non-monotonous behaviour of permeability with respect to the same porogen vol% is observed. Fig. 12a illustrates the distribution of the database (as 'O' in black) and validation points (as diamond shapes in red, blue, and green) on the valid process region, with diagonal lines indicating 30, 50, and 60 vol% porogen. As illustrated in Fig. 13b, the influence of pore size and microcracks generated by the porogens on permeability is particularly evident at lower porogen contents. Samples prepared with the larger porogen (100–200) exhibit higher permeability than those made with the smaller porogen (25–100) at the same vol%. This can be explained by observing that the two different porogen sizes differ mostly by scale (see Fig. 4). And the scale effect for permeability is analytic: the permeability is proportional to the square of the microstructure's characteristic length. With increasing porogen content, this effect, however becomes less pronounced. Furthermore, for a mixed-porogen composition of approximately 60 vol % (combining 25–100 and 100–200 porogens equally), the measured permeability exceeds that of the other samples, apparently due to an interactive effect arising from the bimodal pore size distribution, which is absent at lower porogen contents. Also, observing Figs. 4e and 4f, we can see that 4e has higher coalescence compared to 4 f. To the authors' knowledge, this phenomenon has not been explained yet from a theoretical perspective and deserves further investigation. Additionally, as a non-definitive observation, we note that the extent of incomplete resin infusion into the samples for polishing varies with the material's porosity and pore connectivity. This pattern indicates that microstructural characteristics could affect the consistency of resin penetration.

5. Conclusion

This research focuses on the fabrication of porous, permeable alumina ceramics using the sacrificial template technique. The influence of porogen size and volume percentage on the sample permeability and mechanical resistance is well documented in the literature. However, the characterization of the process parameters' limits to obtain a viable sample (permeable and not fractured) is not systematically studied, necessitating experimental determination for each case. To address this problem, we developed a batch active learning algorithm based on Gaussian process classification (GPC) to iteratively determine the viable domain with a limited set of experimental data. One of the main developments of this study is to work with a batch mode, allowing to manufacture and test several samples in parallel, which is of particular interest for the powder metallurgy process. In this study, we demonstrated the approach with two parameters as a proof of concept to visualize the model's response. However, the goal of this development is to address more complex problems where identifying the optimal experimental conditions is not intuitive. For instance, numerous process parameters such as porogen with different shapes and sizes, debinding and sintering ramp temperature, compaction loads, etc. The scaling challenges associated with extending the model to higher-dimensional parameter spaces are outlined in Annex G of the supplementary material.

Thanks to a carefully designed permeability bench, the fine interplay between porogen size and vol% is highlighted: At low volume

percentage, the smaller the porogens, the lower the permeability, which is explained by the theory of permeability. And at high vol%, the trend is less obvious, and the higher permeability is obtained for a 50/50 mixture. This finding is hard to explain theoretically and would require more investigation. In the identified viable domain, a Gaussian process regression (GPR) model is implemented to predict the permeability of defined process parameter samples. The GPR model captures the non-monotonous relationship between porogen parameters (vol% and size) and resulting permeability, allowing for quantitative prediction of material properties.

This work provides a technical demonstration of a data-driven process–property model with quantitative predictive capabilities. Although such models do not, by themselves, yield new physical insight, they offer a powerful framework for investigating underlying mechanisms as a perspective of this work. Here, we focused on the influence of porogen content on permeability and mechanical integrity to highlight the potential of our batch active-learning strategy. It must be noted that this back-and-forth model-experiment methodology is not broadly used in experimental material science. The developed active learning algorithm and GPR model can thus be generalised to any manufacturing method, particularly for processes with a limited amount of material available or high-cost experiments (nuclear industry, aeronautics). Finally, we intend to develop a regression model relating pore morphology to permeability and to compare our results with the existing parametric correlation equations [56] relating permeability to porosity, pore size, pore throat size, and connectivity. Interesting experimental studies have been conducted to compare pore structure and permeability [57].

The toolkit developed for building the presented models and the active-learning procedure is made available in a GitLab repository [42].

CRediT authorship contribution statement

Renaud Ferrier: Writing – review & editing, Visualization, Validation, Supervision, Software, Resources, Methodology, Investigation, Funding acquisition, Formal analysis, Data curation, Conceptualization. **Paul Baral:** Writing – review & editing, Visualization, Validation, Supervision, Software, Resources, Methodology, Investigation, Funding acquisition, Formal analysis, Data curation, Conceptualization. **Liam Latour:** Visualization, Software, Methodology, Investigation, Conceptualization. **Jnanesh Gopale Gowda:** Writing – review & editing, Writing – original draft, Visualization, Validation, Software, Methodology, Investigation, Formal analysis, Data curation, Conceptualization. **Sébastien Saunier:** Writing – review & editing, Visualization, Validation, Supervision, Resources, Project administration, Methodology, Investigation, Funding acquisition, Formal analysis, Data curation, Conceptualization.

Declaration of Competing Interest

The authors declare that they have no known competing financial interests or personal relationships that could have appeared to influence the work reported in this paper.

Appendix A. Supporting information

Supplementary data associated with this article can be found in the online version at doi:10.1016/j.jeurceramsoc.2025.118116.

References

[1] A.J. Langhammer, Powder Metallurgy: Its Physics and Production. Paul Schwarzkopf, Science 107 (1948) 515–516, https://doi.org/10.1126/science.107.2785.515.b.

[2] E.C. Hammel, O.L.-R. Ighodaro, O.I. Okoli, Processing and properties of advanced porous ceramics: An application based review, Ceram. Int. 40 (2014) 15351–15370, https://doi.org/10.1016/j.ceramint.2014.06.095.

[3] T. Ohji, M. Fukushima, Macro-porous ceramics: processing and properties, Int. Mater. Rev. 57 (2012) 115–131, https://doi.org/10.1179/1743280411Y.0000000006.

[4] D. Santo, M. Rodarte, C. Andreto, D. Cavaleiro, I. Carvalho, R. Balestra, S. Carvalho, Multifunctional alumina scaffolds with enhanced bioactivity and antimicrobial properties for bone tissue engineering, Ceram. Int. 51 (2025) 6155–6165, https://doi.org/10.1016/j.ceramint.2024.12.059.

[5] R. Macías, L. Olmos, P. Garnica, I. Alanis, D. Bouvard, J. Chávez, O. Jiménez, C. Márquez-Beltrán, J.L. Cabezas-Vila, Processing of Porous-Core Materials for Bone Implant Applications: A Permeability and Mechanical Strength Analysis, Coatings 14 (2024) 65, https://doi.org/10.3390/coatings14010065.

[6] M. Chen, S.G.J. Heijman, L.C. Rietveld, State-of-the-Art Ceramic Membranes for Oily Wastewater Treatment: Modification and Application, Membr. (Basel) 11 (2021) 888, https://doi.org/10.3390/membranes11110888.

[7] L. Zhu, K.P. Rakesh, M. Xu, Y. Dong, Ceramic-Based Composite Membrane with a Porous Network Surface Featuring a Highly Stable Flux for Drinking Water Purification, Membr. (Basel) 9 (2019) 5, https://doi.org/10.3390/membranes9010005.

[8] Y. Chen, N. Wang, O. Ola, Y. Xia, Y. Zhu, Porous ceramics: Light in weight but heavy in energy and environment technologies, Materials Science Engineering R Reports 143 (2021) 100589, https://doi.org/10.1016/j.mser.2020.100589.

[9] S. Chugunov, A. Kazak, M. Amro, C. Freese, I. Akhatov, Towards Creation of Ceramic-Based Low Permeability Reference Standards, Mater. (Basel) 12 (2019) 3886, https://doi.org/10.3390/ma12233886.

[10] M. Dutto, D. Goeuriot, S. Saunier, S. Marinel, N. Frage, S. Hayun, Reaction-bonded B4C/SiC composites synthesized by microwave heating, Int. J. Appl. Ceram. Technol. 16 (2019) 1287–1294, https://doi.org/10.1111/ijac.13211.

[11] X. Zhou, S. Liu, J. Chen, L. Zhu, X. Tong, Z. Chen, Y. Li, J. Lin, C. Wen, J. Ma, Enamel-like Polymer-Infiltrated Ceramic Materials for Dental Applications, J. Dent. Res 104 (2025) 629–636, https://doi.org/10.1177/00220345251313998.

[12] A. Dutto, M. Zanini, E. Jeoffroy, E. Tervoort, S.A. Mhatre, Z.B. Seibold, M. Bechthold, A.R. Studart, 3D Printing of Hierarchical Porous Ceramics for Thermal Insulation and Evaporative Cooling, Adv. Mater. Technol. 8 (2023) 2201109, https://doi.org/10.1002/admt.202201109.

[13] G. Jean, V. Sciamanna, M. Demuynck, F. Cambier, M. Gonon, Macroporous ceramics: Novel route using partial sintering of alumina-powder agglomerates obtained by spray-drying, Ceram. Int. (2014), https://doi.org/10.1016/j.ceramint.2014.02.089.

[14] A. Pokhrel, D.N. Seo, S.T. Lee, I.J. Kim, Processing of Porous Ceramics by Direct Foaming: A Review, J. Korean Ceram. Soc. 50 (2013) 93–102, https://doi.org/10.4191/kcers.2013.50.2.093.

[15] V.R. Salvini, B. Luchini, C.G. Aneziris, V.C. Pandolfelli, Innovation in ceramic foam filters manufacturing process, Int. J. Appl. Ceram. Technol. 16 (2019) 378–388, https://doi.org/10.1111/ijac.13062.

[16] M. Ciurans Oset, J. Nordin, F. Akhtar, Processing of Macroporous Alumina Ceramics Using Pre-Expanded Polymer Microspheres as Sacrificial Template, Ceramics 1 (2018) 329–342, https://doi.org/10.3390/ceramics1020026.

[17] S. Li, C.-A. Wang, J. Zhou, Effect of starch addition on microstructure and properties of highly porous alumina ceramics, Ceram. Int. 39 (2013) 8833–8839, https://doi.org/10.1016/j.ceramint.2013.04.072.

[18] J. Alzukaimi, R. Jabrah, Development of high strength large open porosity alumina ceramics using the sacrificial phase route: The role of the sacrificial phase fineness, Ceram. Int. 49 (2023) 2923–2933, https://doi.org/10.1016/j.ceramint.2022.09.277.

[19] C.E. Rasmussen, C.K.I. Williams, Gaussian processes for machine learning, 3. print, MIT Press, Cambridge, Mass, 2006.

[20] N. Roy, A. McCallum, Toward Optimal Active Learning through Sampling Estimation of Error Reduction, in: Proceedings of the Eighteenth International Conference on Machine Learning, Morgan Kaufmann Publishers Inc, San Francisco, CA, USA, 2001, pp. 441–448.

[21] W. Cai, Y. Zhang, J. Zhou, Maximizing Expected Model Change for Active Learning in Regression, 2013. https://doi.org/10.1109/ICDM.2013.104.

[22] D.D. Lewis, W.A. Gale, in: B.W. Croft, C.J. Van Rijsbergen (Eds.), A Sequential Algorithm for Training Text Classifiers, Springer, London, 1994, pp. 3–12, https://doi.org/10.1007/978-1-4471-2099-5_1.

[23] Y. Li, E. Jiang, Z. Ni, W. Li, M. Huang, F. Zhao, F. Liu, Y. Ye, S. Bai, A study of the role of data and model uncertainty in active learning, Comput. Mater. Sci. 247 (2025) 113512, https://doi.org/10.1016/j.commatsci.2024.113512.

[24] W. Cai, M. Zhang, Y. Zhang, Batch Mode Active Learning for Regression With Expected Model Change, IEEE Trans. Neural Netw. Learn. Syst. 28 (2017) 1668–1681, https://doi.org/10.1109/TNNLS.2016.2542184.

[25] T.N.C. Cardoso, R.M. Silva, S. Canuto, M.M. Moro, M.A. Gonçalves, Ranked batch-mode active learning, Inf. Sci. 379 (2017) 313–337, https://doi.org/10.1016/j.ins.2016.10.037.

[26] S.M. Shah, J. Yang, J.P. Crawshaw, O. Gharbi, E.S. Boek, Predicting Porosity and Permeability of Carbonate Rocks From Core-Scale to Pore-Scale Using Medical CT, Confocal Laser Scanning Microscopy and Micro CT, in: OnePetro, 2013, https://doi.org/10.2118/166252-MS.

[27] M. Mahdaviara, A. Rostami, F. Keivanimehr, K. Shahbazi, Accurate determination of permeability in carbonate reservoirs using Gaussian Process Regression, J. Pet. Sci. Eng. 196 (2021) 107807, https://doi.org/10.1016/j.petrol.2020.107807.

[28] S. Asante-Okyere, C. Shen, Y.Y. Ziggah, M.M. Rulegeya, X. Zhu, Investigating the Predictive Performance of Gaussian Process Regression in Evaluating Reservoir Porosity and Permeability, Energies 11 (2018) 1–13.

[29] J. Cai, X. Chu, K. Xu, H. Li, J. Wei, Machine learning-driven new material discovery, Nanoscale Adv 2 (n.d.) 3115–3130. https://doi.org/10.1039/d0na00388c.
[30] O. Ozbayram, A. Olivier, L. Graham-Brady, Heteroscedastic Gaussian Process Regression for material structure–property relationship modeling, Comput. Methods Appl. Mech. Eng. 431 (2024) 117326, https://doi.org/10.1016/j.cma.2024.117326.
[31] D. Jiang, Z. Wang, J. Zhang, D. Jiang, F. Liu, L. Hao, Predictive modelling for contact angle of liquid metals and oxide ceramics by comparing Gaussian process regression with other machine learning methods, Ceram. Int. 48 (2022) 665–673, https://doi.org/10.1016/j.ceramint.2021.09.146.
[32] D. Lee, M. Ruf, N. Karadimitriou, H. Steeb, M. Manousidaki, E.A. Varouchakis, S. Tzortzakis, A. Yiotis, Development of stochastically reconstructed 3D porous media micromodels using additive manufacturing: numerical and experimental validation, Sci. Rep. 14 (2024) 9375, https://doi.org/10.1038/s41598-024-60075-w.
[33] Y. Zhang, H. Li, A. Abdelhady, J. Yang, Comparative laboratory measurement of pervious concrete permeability using constant-head and falling-head permeameter methods, Constr. Build. Mater. 263 (2020) 120614, https://doi.org/10.1016/j.conbuildmat.2020.120614.
[34] G.F.B. Sandoval, I. Galobardes, R.S. Teixeira, B.M. Toralles, Comparison between the falling head and the constant head permeability tests to assess the permeability coefficient of sustainable Pervious Concretes, Case Stud. Constr. Mater. 7 (2017) 317–328, https://doi.org/10.1016/j.cscm.2017.09.001.
[35] M. Hassanabadi, T. Berto, S. Akhtar, R.E. Aune, Hydraulic Characterization of Ceramic Foam Filters Used in Aluminum Filtration, Materials 16 (2023) 2805, https://doi.org/10.3390/ma16072805.
[36] E.A. Moreira, M. Innocentini, J.R. Coury, Permeability of Ceramic Foams to Compressible and Incompressible Flow, J. EUR. CERAM. SOC. J. EUR CERAM SOC 24 (2004) 3209–3218, https://doi.org/10.1016/j.jeurceramsoc.2003.11.014.
[37] A.X.H. Yong, A. Endruweit, A. George, D. May, Y.A. Aksoy, M.A. Ali, T. Allen, P. Baral, C. Betteridge, C. Brauner, B. Caglar, A. Chiminelli, D. Cracknell, L. Dame, J. Dittmann, C. Dransfeld, S. Drapier, J.A. García Manrique, E. Garrigou, A. Guilloux, P. Hubert, J. Ivens, J. Janzen, T. Khan, H. Kikuta, K. Kind, M. Laspalas, J. Lee, X. Liu, M. Lizaranzu, S.V. Lomov, K. Masania, V. Michaud, P. Middendorf, S. Miguel, J. Muñoz, S.S. Narayana, C.H. Park, G. Pedoto, A. Pisupati, D. Sayinbas, P. Sousa, M. Sozer, J. Staal, M. Steinhardt, H. Teixido, R. Umer, J.D. Vincent, V. Werlen, O. Yuksel, Towards standardisation of the out-of-plane permeability measurement for reinforcement textiles, Composites Part A Applied Science Manufacturing 190 (2025) 108630, https://doi.org/10.1016/j.compositesa.2024.108630.
[38] Y. Yang, F. Liu, Q. Chang, Z. Hu, Q. Wang, Y. Wang, Preparation of Fly Ash-Based Porous Ceramic with Alumina as the Pore-Forming Agent, Ceramics 2 (2019) 286–295, https://doi.org/10.3390/ceramics2020023.
[39] L. Breiman, Random Forests, Mach. Learn. 45 (2001) 5–32, https://doi.org/10.1023/A:1010933404324.
[40] C. Cortes, V. Vapnik, Support-vector networks, Mach. Learn 20 (1995) 273–297, https://doi.org/10.1007/BF00994018.
[41] scikit-learn: machine learning in Python — scikit-learn 1.6.0 documentation, (n.d.). ⟨https://scikit-learn.org/stable/index.html⟩ (accessed December 30, 2024).
[42] Renaud FERRIER / processMapper · GitLab, GitLab (2025). ⟨https://gitlab.emse.fr/renaud.ferrier/processmapper⟩ (accessed October 7, 2025).
[43] GaussianProcessClassifier, Scikit-Learn (n.d.). ⟨https://scikit-learn/stable/modules/generated/sklearn.gaussian_process.GaussianProcessClassifier.html⟩ (accessed December 30, 2024).
[44] D. Khatamsaz, B. Vela, P. Singh, D.D. Johnson, D. Allaire, R. Arróyave, Multi-objective materials bayesian optimization with active learning of design constraints: Design of ductile refractory multi-principal-element alloys, Acta Mater. 236 (2022) 118133, https://doi.org/10.1016/j.actamat.2022.118133.
[45] D. Khatamsaz, V. Attari, R. Arróyave, Microstructure-aware Bayesian materials design, Acta Mater. 303 (2026) 121587, https://doi.org/10.1016/j.actamat.2025.121587.
[46] Q. Wei, Y. Wang, G. Yang, T. Li, S. Yu, Z. Dong, T.-Y. Zhang, Discovering novel lead-free solder alloy by multi-objective Bayesian active learning with experimental uncertainty, Npj Comput. Mater. 11 (2025) 10, https://doi.org/10.1038/s41524-024-01480-7.
[47] Y. Xian, P. Dang, Y. Tian, X. Jiang, Y. Zhou, X. Ding, J. Sun, T. Lookman, D. Xue, Compositional design of multicomponent alloys using reinforcement learning, Acta Mater. 274 (2024) 120017, https://doi.org/10.1016/j.actamat.2024.120017.
[48] A.M. Faizan Mohamed, F. Careri, R.H.U. Khan, M.M. Attallah, L. Stella, A novel porosity prediction framework based on reinforcement learning for process parameter optimization in additive manufacturing, Scr. Mater. 255 (2025) 116377, https://doi.org/10.1016/j.scriptamat.2024.116377.
[49] K. Wang, M. Qiu, C. Jiao, J. Gu, D. Xie, C. Wang, X. Tang, Z. Wei, L. Shen, Study on defect-free debinding green body of ceramic formed by DLP technology, Ceram. Int. 46 (2020) 2438–2446, https://doi.org/10.1016/j.ceramint.2019.09.237.
[50] K. Kamitani, T. Hyodo, Y. Shimizu, M. Egashira, Fabrication of Highly Porous Alumina-Based Ceramics with Connected Spaces by Employing PMMA Microspheres as a Template, Adv. Mater. Sci. Eng. 2009 (2009) 601850, https://doi.org/10.1155/2009/601850.
[51] M.S. Ali, M.A.A. Hanim, S.M. Tahir, C.N.A. Jaafar, M. Norkhairunnisa, K.A. Matori, Preparation and characterization of porous alumina ceramics using different pore agents, J. Ceram. Soc. Jpn. 125 (2017) 402–412, https://doi.org/10.2109/jcersj2.16233.
[52] J. Du, D. Ai, X. Xiao, J. Song, Y. Li, Y. Chen, L. Wang, K. Zhu, Rational Design and Porosity of Porous Alumina Ceramic Membrane for Air Bearing, Membr. (Basel) 11 (2021) 872, https://doi.org/10.3390/membranes11110872.
[53] L. Biasetto, P. Colombo, M.D.M. Innocentini, S. Mullens, Gas Permeability of Microcellular Ceramic Foams, Ind. Eng. Chem. Res. 46 (2007) 3366–3372, https://doi.org/10.1021/ie061335d.
[54] J. Seuba, S. Deville, C. Guizard, A.J. Stevenson, Gas permeability of ice-templated, unidirectional porous ceramics, Sci. Technol. Adv. Mater. 17 (2016) 313–323, https://doi.org/10.1080/14686996.2016.1197757.
[55] A.D. Kiureghian, O. Ditlevsen, Aleatory or epistemic? Does it matter? Struct. Saf. 31 (2009) 105–112, https://doi.org/10.1016/j.strusafe.2008.06.020.
[56] J. Cai, Z. Zhang, W. Wei, D. Guo, S. Li, P. Zhao, The critical factors for permeability-formation factor relation in reservoir rocks: Pore-throat ratio, tortuosity and connectivity, Energy 188 (2019) 116051, https://doi.org/10.1016/j.energy.2019.116051.
[57] W. Chen, K. Li, M. Wu, D. Liu, P. Wang, Y. Liang, Influence of pore structure characteristics on the gas permeability of concrete, J. Build. Eng. 79 (2023) 107852, https://doi.org/10.1016/j.jobe.2023.107852.